FDwave3D: A MATLAB solver for the 3D anisotropic wave equation using the finite-difference method

Lei Li[1, 2, 3], Jingqiang Tan[1, 2, 3*], Dazhou Zhang[1, 2, 3*], Ajay Malkoti[4], Ivan Abakumov[5], Yujiang Xie[6]

1 Key Laboratory of Metallogenic Prediction of Nonferrous Metals and Geological Environment Monitoring (Central South University), Ministry of Education, 410083 Changsha, China

2 Hunan Key Laboratory of Nonferrous Resources and Geological Hazard Exploration, 410083 Changsha, China

3 School of Geosciences and Info-Physics, Central South University, 410083 Changsha, China

4 Tata Institute of Fundamental Research, Mumbai 400005, India

5 Geophysics Section, Earth Science Department, Freie Universität Berlin, 12249 Berlin, Germany

6 Ocean and Earth Science, University of Southampton, SO14 3ZH Southampton, United Kingdom

* Corresponding author. J Tan and D Zhang share the corresponding author.

Email address: tanjingqiang@gmail.com (J. Tan), dazhou2005@163.com (D. Zhang) , leileely@126.com (L. Li)

ORCiD:

Lei Li: 0000-0002-3391-5608

Jingqiang Tan: 0000-0002-7015-0528

Dazhou Zhang: 0000-0002-0765-1055

Ajay Malkoti: 0000-0002-7436-3627

Conflicts of interest

We declare no conflicts of interests.

Code availability

The code package *FDwave3D* is available in MATLAB on GitHub at https://github.com/leileely/FDwave3D .

Authors' contributions

L. Li contributed to method development and testing, and drafted the manuscript. J. Tan contributed to manuscript review and funding acquisition. D. Zhang, A. Malkoti, I. Abakumov, and Y. Xie contributed to code programming, testing, and revised the manuscript.

Abstract

Seismic modeling plays an important role in geophysics and seismology for estimating the response of seismic sources in a given medium. In this work, we present a MATLAB-based package, *FDwave3D,* for synthetic wavefield and seismogram modeling in 3D anisotropic media. The seismic simulation is carried out using the finite-difference method over the staggered grid, and it is applicable to both active and passive surveys. The code package allows the incorporation of arbitrary source mechanisms and offers spatial derivative operators of accuracy up to tenth-order along with different types of boundary conditions. First, the methodological aspects of finite-difference method are briefly introduced. Then, the code has been tested and verified against the analytical solutions obtained for the homogeneous model. Further, the numerical examples of layered and overthrust models are presented to demonstrate its reliability.

Nomenclature

FDM	Finite-difference method	n	Time step
VTI	Vertical transverse isotropic	M	Half of the order of FD operator
HTI	Horizontal transverse isotropic	c_m	FD coefficients
PML	Perfectly matched layer	u_i	Displacement
TI	Transverse isotropic	$\mathbf{M}$	Moment tensor
FD	Finite difference	m_{ij}	Moment tensor components
RMS	Root-mean-square	$G_{ij,k}$	Spatial derivative of the Green's function
ρ	Density	$s(t)$	Source-time function
v_i	Particle velocity	$\dot{s}(t)$	Derivative of the source-time function
τ_{ij}	Stress	V_P	P-wave velocity
ε_{ij}	Strain	V_S	S-wave velocity
f_i	Body force	γ_i	Direction cosine of the ray path
C_{ijkl}	Tensor of elastic moduli	δ_{ij}	The Kronecker delta function
C_{ij}	Second-order components of elastic moduli	V	Volume of a grid cell
λ	Lame constant	$\Delta\tau_{ij}$	The incremental stress
μ	Shear modulus	α	Damping parameter
α_0	P-wave velocity along the respective axis	$V_{\max}$	Maximum velocity along all directions
β_0	S-wave velocity along the respective axis	$V_{\min}$	Minimum velocity along all directions
$\varepsilon,\gamma,\delta$	Thomsen's anisotropy parameters	nt	Total number of time steps
$dh/dx/dy/dz$	Space interval	$\lambda_{\min}$	Minimum wavelength
dt	Time interval	$f_{\max}$	Maximum frequency of the source signal
D^+	Forward derivative operator		
D^-	Backward derivative operator		

1 Introduction

In recent years, both the academic and industrial communities have shown an increasing interest in passive seismic, such as microseismic monitoring. For active seismic surveys, the seismic anisotropic effect is often ignored to accelerate the simulation of seismic wavefields, and an explosive or force source is generally used to mimic explosives or seismic sources from trucks [1]. For microseismic monitoring, seismic anisotropy has significant effects on the recorded traveltime and amplitudes, and increases the uncertainty for source location [2] and source mechanism inversion [3]. The source

4

mechanism can provide fundamental information to understand the rock failure process, and it also lays the foundation for subsequent geomechanical analyses and geological interpretations. In the context of passive seismic monitoring, both double-couple and non-double-couple source mechanisms are observed [4, 5]. Various researchers have shown that the processing and interpretation of microseismic data can be greatly facilitated by seismic wavefield modeling [6–8].

Seismic forward modeling can be used to obtain the seismic response of a source(s) with a defined mechanism within the given medium (e.g., anisotropic or attenuative media) [9, 10]. The exact analytical solutions of wave equations do not exist for complex subsurface configurations, and numerical methods such as the finite-difference method (FDM) play a vital role in such cases [10–13]. The FDM transforms the set of the partial differential equations, that govern the propagation of seismic waves within the media, into a system of algebraic equations through its discretization over the computational domain. A large amount of effort has been put into the development of various aspects of FDM, including rheology [14, 15], grid schemes [16, 17], and boundaries [18–20]. The FDM is based on the complete wave equation (with least physical approximations) and it can account for relative amplitudes of various arrivals (e.g., primaries and multiples). Seismic anisotropy is characterized by the elastic parameters and can be incorporated into FDM through the elastic wave equation [21]. Here we take the two commonly-used anisotropic media, vertical transverse isotropic (VTI) and horizontal transverse isotropic (HTI) media, as examples to showcase the anisotropic effects. The moment tensor source can be implemented by adding increments on the stress or particle velocity components [22, 23].

From the perspective of code availability, most of the current open-source packages are in C and FORTRAN, and some are limited to 2D cases [24–26]. A list of available codes for simulating seismic wave propagation is summarized in Table 1. During the last decades, MATLAB has emerged as a preferred platform for carrying out the scientific simulations due to its features and advantages, such as the dynamical expansion of matrices, strong interactive experience and parallel computing performance, flexible declaration and allocation of variables [12, 27]. Though there are several MATLAB-based seismic packages or tools, such as SplitLab [28] and Crazyseismic [29], only a few packages are available for seismic wave simulation in 2D scenarios [26, 30].

In this work, we have developed a MATLAB solver (*FDwave3D*) for seismic forward modeling, which is an extension of the previous code package *FDwave* [26]. Since the computational power of modern computers enables us to simulate full seismic wavefields for large and complex 3D models, we leverage it to provide a concise, comprehensible, and practical framework of 3D wavefield modeling in anisotropic media. The unique capabilities of the *FDwave3D* package are: (1) variable order accuracy of spatial derivative (up to tenth-order) using the staggered grid, (2) incorporation of arbitrary source mechanisms using the moment tensor, (3) option for different types of absorbing boundary conditions, i.e., perfectly matched layer (PML) and damped boundary condition, and (4) efficient implementation using vectorization. The code package is suitable for anisotropic elastic wave propagation simulation in both active and passive seismic surveys. We have provided numerical examples of 3D anisotropic models to demonstrate the reliability of the code package.

Table 1

Representative FD codes for seismic wave modeling. VS and DS represent velocity-stress formulation and displacement-stress formulation, respectively. "/" denotes no parallelization implementation.

Rheology	Scheme	Grid type	Parallelization	Language	References
Viscoelastic	VS	Staggered	MPI	C	[14]
Poroelastic	VS	Staggered	MPI	C	[24]
Anisotropic elastic	DS	Collocated	/	Matlab	[30]
Viscoelastic	VS	Staggered	MPI+OpenMP	Fortran	[31]
Elastic	VS	Staggered	GPU	CUDA	[32]
Viscoelastic	VS	Staggered	OpenMP	C	[25]
Anisotropic elastic	DS	Collocated	GPU+OpenMP	CUDA	[33]
Elastic	VS	Staggered	MPI	C	[34]
Elastic	VS	Staggered	GPU	CUDA	[35]
Viscoelastic	VS	Staggered	MPI+OpenMP	Fortran	[36]
Viscoelastic	VS	Staggered	GPU	OpenCL	[37]
Anisotropic viscoelastic	DS	Collocated	/	C	[38]
Anisotropic elastic	VS	Staggered	OpenMP	Fortran	[39]
Elastic	VS	Staggered	Vectorized	Matlab	[26]
Anisotropic elastic	VS	Staggered	Vectorized	Matlab	This study

2 Methodology

In this section, we briefly discuss the basic theory and methodology required for numerical simulation of seismic wave propagation using FDM, which includes the elastic wave formulation, discretization strategies, boundary conditions, and stability and dispersion issues. More detailed descriptions of the theory and workflow of FDM can be found in [9] and [10].

2.1 Elastic wave modeling using the finite-difference method

The basic equations for elastodynamic wave motion include the momentum conservation equation (equation of motion) and the constitutive law (Hooke's law) which specifies the relation between the stress and strain tensors. These two equations for generally anisotropic elastic media can be written as

$$\rho \frac{\partial v_i}{\partial t} = \frac{\partial \tau_{ij}}{\partial x_j} + f_i, \tag{1}$$

$$\tau_{ij} = C_{ijkl} \varepsilon_{kl}, \tag{2}$$

where ρ is the density of the medium, v_i is the particle velocity, $\tau_{ij}, \varepsilon_{kl}$ are the stresses and strains, f_i is the external body force in the direction i, C_{ijkl} denotes the tensor of elastic moduli, and $i, j, k, l \in \{x, y, z\}$. Subscripts in the equation follow the Einstein summation convention. Owing to the symmetry of stress and strain components, the fourth-order elastic tensor can be reduced to second-order tensor following the Voigt notation [40]. The elastic tensor has only 21 independent

8

parameters in a general and full anisotropic medium and the complete equation of Hook's is

$$
\begin{pmatrix} \tau_{xx} \\ \tau_{yy} \\ \tau_{zz} \\ \tau_{yz} \\ \tau_{xz} \\ \tau_{xy} \end{pmatrix} = \begin{pmatrix} C_{11}, C_{12}, C_{13}, C_{14}, C_{15}, C_{16} \\ C_{12}, C_{22}, C_{23}, C_{24}, C_{25}, C_{26} \\ C_{13}, C_{23}, C_{33}, C_{34}, C_{35}, C_{36} \\ C_{14}, C_{24}, C_{34}, C_{44}, C_{45}, C_{46} \\ C_{15}, C_{25}, C_{35}, C_{45}, C_{55}, C_{56} \\ C_{16}, C_{26}, C_{36}, C_{46}, C_{56}, C_{66} \end{pmatrix} \begin{pmatrix} \varepsilon_{xx} \\ \varepsilon_{yy} \\ \varepsilon_{zz} \\ \varepsilon_{yz} \\ \varepsilon_{xz} \\ \varepsilon_{xy} \end{pmatrix}, \quad (3)
$$

where τ_{ij} are ε_{ij} stress and strain components, and $i, j \in \{x, y, z\}$. For the transverse isotropy case, only 5 independent components are involved, which are $C_{11}, C_{13}, C_{33}, C_{44}, C_{66}$, and $C_{12} = C_{11} - 2C_{66}$. The isotropic case can be obtained from the transversely isotropic case, where $C_{11} = C_{33} = \lambda + 2\mu$, $C_{44} = C_{66} = \mu$, and $C_{13} = \lambda$, in terms of two independent Lame's constants λ and μ. The tensor of elastic moduli for the transversely isotropic and isotropic media are given by

$$
\mathbf{C}(\text{transversely isotropic}) = \begin{pmatrix} C_{11}, C_{12}, C_{13}, & 0, & 0, & 0 \\ C_{12}, C_{11}, C_{13}, & 0, & 0, & 0 \\ C_{13}, C_{13}, C_{33}, & 0, & 0, & 0 \\ 0, & 0, & 0, & C_{44}, & 0, & 0 \\ 0, & 0, & 0, & 0, & C_{44}, & 0 \\ 0, & 0, & 0, & 0, & 0, & C_{66} \end{pmatrix} \quad (4)
$$

$$
\mathbf{C}(\text{isotropic}) = \begin{pmatrix} \lambda+2\mu, \lambda, \lambda, & 0, & 0, & 0 \\ \lambda, \lambda+2\mu, \lambda, & 0, & 0, & 0 \\ \lambda, \lambda, \lambda+2\mu, & 0, & 0, & 0 \\ 0, & 0, & 0, & \mu, & 0, & 0 \\ 0, & 0, & 0, & 0, & \mu, & 0 \\ 0, & 0, & 0, & 0, & 0, & \mu \end{pmatrix}, \quad (5)
$$

The Lame's parameters are preferred since these two are directly related to the P- and S-wave velocities. It makes more sense to choose the parameters with a physical interpretation, and thereby, the anisotropy parameters are generally expressed using the Thomsen's parameters $(\varepsilon, \gamma, \delta)$ and two velocities (α_0, β_0) to characterize weak anisotropy in exploration seismology, and the relations between the five parameters and elastic moduli are [41]

$$
\begin{cases}
\alpha_0 = \sqrt{\dfrac{C_{33}}{\rho}} \\[2mm]
\beta_0 = \sqrt{\dfrac{C_{44}}{\rho}} \\[2mm]
\varepsilon = \dfrac{C_{11} - C_{33}}{2C_{33}} \\[2mm]
\gamma = \dfrac{C_{66} - C_{44}}{2C_{44}} \\[2mm]
\delta = \dfrac{\left(C_{13} + C_{44}\right)^2 - \left(C_{33} - C_{44}\right)^2}{2C_{33}\left(C_{33} - C_{44}\right)}
\end{cases}
. \quad (6)
$$

The α_0 and β_0 are related to P-wave and S-wave velocity parallel to the respective axis, whereas ε and γ reflect the fractional change in the P-wave and S-wave velocities, respectively.

2.2 Finite difference formulation for elastic wave simulation

The strain rate can be defined as $\partial \varepsilon_{ij} / \partial t = 1/2 \left(\partial v_i / \partial x_j + \partial v_j / \partial x_i \right)$ and substituting this definition into the time derivative of Hooke's law, we obtain the velocity-stress formulation as a coupled partial differential equation (PDE), which is adopted in the present work. The set of the coupled PDE obtained above is discretized over the staggered grid, which is quite frequently used for the 3D FD modeling of seismic wave propagation and earthquake motion [16, 22, 42, 23]. The arrangement of the material

parameters (e.g., density, velocity) and field parameters (e.g., stresses and particle velocities) for the staggered grid and the collocated grid are shown in Figure 1. The parameters on the staggered grid are positioned on different nodes separated by half the grid spacing, which increases the accuracy and stability of the FDM. A disadvantage of staggered grids is that the off-diagonal stress and strain components are not defined and computed in the same position. Therefore, some stress components have to be interpolated, which accounts for stress-strain relation [43] and moment tensor source implementation [39].
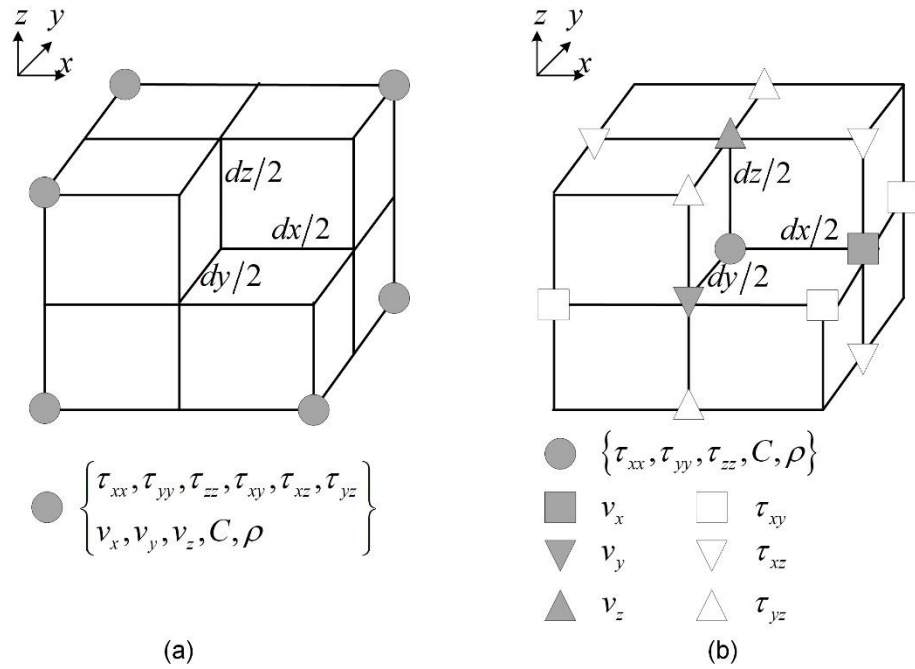

Figure 1. Schematic representations of (a) the collocated grid (a) and (b) the staggered grid (b). The staggered-grid implementation is realized by shifting half spacing of the conventional full grid and overlapping meshes of individual components.

The velocity-stress formulation shown in anisotropic media can be discretized over the standard staggered grid as follows [14, 39]

$$\begin{cases} v_x \big|^n = v_x \big|^{n-1} + \dfrac{dt}{\rho}\left(D_x^+ \tau_{xx} \big|^{n-} + D_y^- \tau_{xy} \big|^{n-} + D_z^- \tau_{xz} \big|^{n-} \right) \\[2mm] v_y \big|^n = v_y \big|^{n-1} + \dfrac{dt}{\rho}\left(D_y^+ \tau_{yy} \big|^{n-} + D_x^- \tau_{xy} \big|^{n-} + D_z^- \tau_{yz} \big|^{n-} \right) \\[2mm] v_z \big|^n = v_z \big|^{n-1} + \dfrac{dt}{\rho}\left(D_z^+ \tau_{zz} \big|^{n-} + D_x^- \tau_{xz} \big|^{n-} + D_y^- \tau_{yz} \big|^{n-} \right) \end{cases} \qquad (7)$$

$$\begin{cases} \tau_{xx} \big|^{n+} = \tau_{xx} \big|^{n-} + dt \left[\begin{array}{l} \left(C_{11}D_x^- + C_{15}D_z^- + C_{16}D_y^-\right)v_x \big|^n + \left(C_{12}D_y^- + C_{14}D_z^- + C_{16}D_x^-\right)v_y \big|^n \\ \qquad + \left(C_{13}D_z^- + C_{14}D_y^- + C_{15}D_x^-\right)v_z \big|^n \end{array} \right] \\[4mm] \tau_{yy} \big|^{n+} = \tau_{xx} \big|^{n-} + dt \left[\begin{array}{l} \left(C_{12}D_x^- + C_{25}D_z^- + C_{26}D_y^-\right)v_x \big|^n + \left(C_{22}D_y^- + C_{24}D_z^- + C_{26}D_x^-\right)v_y \big|^n \\ \qquad + \left(C_{23}D_z^- + C_{24}D_y^- + C_{25}D_x^-\right)v_z \big|^n \end{array} \right] \\[4mm] \tau_{zz} \big|^{n+} = \tau_{xx} \big|^{n-} + dt \left[\begin{array}{l} \left(C_{13}D_x^- + C_{35}D_z^- + C_{36}D_y^-\right)v_x \big|^n + \left(C_{23}D_y^- + C_{34}D_z^- + C_{36}D_x^-\right)v_y \big|^n \\ \qquad + \left(C_{33}D_z^- + C_{34}D_y^- + C_{35}D_x^-\right)v_z \big|^n \end{array} \right] \\[4mm] \tau_{xy} \big|^{n+} = \tau_{xx} \big|^{n-} + dt \left[\begin{array}{l} \left(C_{16}D_x^+ + C_{56}D_z^+ + C_{66}D_y^+\right)v_x \big|^n + \left(C_{26}D_y + C_{46}D_z^+ + C_{66}D_x^+\right)v_y \big|^n \\ \qquad + \left(C_{36}D_z^+ + C_{46}D_y + C_{56}D_x^+\right)v_z \big|^n \end{array} \right] \\[4mm] \tau_{xz} \big|^{n+} = \tau_{xx} \big|^{n-} + dt \left[\begin{array}{l} \left(C_{15}D_x^+ + C_{55}D_z^+ + C_{56}D_y^+\right)v_x \big|^n + \left(C_{25}D_y^+ + C_{45}D_z^+ + C_{56}D_x^+\right)v_y \big|^n \\ \qquad + \left(C_{35}D_z^+ + C_{45}D_y^+ + C_{55}D_x^+\right)v_z \big|^n \end{array} \right] \\[4mm] \tau_{yz} \big|^{n+} = \tau_{xx} \big|^{n-} + dt \left[\begin{array}{l} \left(C_{14}D_x^+ + C_{45}D_z^+ + C_{46}D_y^+\right)v_x \big|^n + \left(C_{24}D_y^+ + C_{44}D_z^+ + C_{46}D_x^+\right)v_y \big|^n \\ \qquad + \left(C_{34}D_z^+ + C_{44}D_y^+ + C_{45}D_x^+\right)v_z \big|^n \end{array} \right] \end{cases} \qquad (8)$$

where C_{ij} is the components of the matrix of elastic moduli and follows the Voigt notation [40]. D^+ and D^- are the shifted discrete derivative operators, which correspond to forward and backward operators, respectively (see equations 9-10 for more details). n^+ and n^- denote $(n+1/2)dt$ and $(n-1/2)dt$, respectively. The remaining parameters have the same meanings as mentioned above.

Our code package offers a dynamic selection from fourth- to tenth-order accurate spatial derivative-based FD schemes. By shifting the coordinate system $\pm 1/2$ grid spacing over the grid, we can obtain the generalized formulation of the forward and backward FD operators as [44]

$$D^+ f(i) = \frac{1}{dh} \sum_{m=1}^{M} c_m \left(f(i+m) - f(i-(m-1)) \right), \tag{9}$$

$$D^- f(i) = \frac{1}{dh} \sum_{m=1}^{M} c_m \left(f(i+(m-1)) - f(i-m) \right), \tag{10}$$

where dh is the spatial spacing, M is the half of the order of FD operator, c_m is the corresponding coefficients for the staggered grid scheme. Please note the operators D^+ and D^- approximate the partial derivative of a continuous function $f(x)$ at $i+1/2$ and $i-1/2$, respectively, since we shift the coordinate system $\pm 1/2$ grid spacing to realize the staggered grid scheme and in real implementations we can only use integers as grid numbers [14].

Here we showcase the sample codes of the transverse isotropy case as Figure 2. The snippets are directly taken from the function *FDwave_calculation_3Delastic_2N_vTI.m* (only the codes of the particle velocity v_x and stress component τ_{xx} are shown).

```
ii=NN+1:nz-NN;
jj=NN+1:nx-NN;
kk=NN+1:ny-NN;

for t=1:Nt

vx_x(ii, jj, kk)=(Pmlxn.*vx_x(ii, jj, kk)+dt*bx(ii, jj, kk).*Dxfm(txx, ii,
jj, kk)/dx)./Pmlxd;
vx_y(ii, jj, kk)=(Pmlyn.*vx_y(ii, jj, kk)+dt*bx(ii, jj, kk).*Dybm(txy, ii,
jj, kk)/dy)./Pmlyd;
vx_z(ii, jj, kk)=(Pmlzn.*vx_z(ii, jj, kk)+dt*bx(ii, jj, kk).*Dzbm(txz, ii,
jj, kk)/dz)./Pmlzd;
……

vx=vx_x+vx_y+vx_z;
……


dxvx = Dxbm(vx,ii, jj, kk)/dx;
dyvy = Dybm(vy,ii, jj, kk)/dy;
dzvz = Dzbm(vz,ii, jj, kk)/dz;

txx_x(ii, jj, kk)=(Pmlxn.*txx_x(ii, jj, kk)+dt*C11(ii, jj, kk).*dxvx)./Pmlxd;
txx_y(ii, jj, kk)=(Pmlyn.*txx_y(ii, jj, kk)+dt*C12(ii, jj, kk).*dyvy)./Pmlyd;
txx_z(ii, jj, kk)=(Pmlzn.*txx_z(ii, jj, kk)+dt*C13(ii, jj, kk).*dzvz)./Pmlzd;
……


txx=txx_x+txx_y+txx_z;
……

end
```

Figure 2. Sample codes of finite difference formulation for elastic wave simulation in transverse isotropy case. Nt and dt are the total number of time steps and time spacing, NN is the half value of the operator order, nx, ny, and nz are the number of spatial nodes in x, y, and z directions, respectively, while dx, dy, and dz are the corresponding spatial spacing. vx_x, vx_y, and vx_z are the components of vx in x, y, and z directions, respectively, and those of txx have similar meanings. Pmlxn and Pmlxd are the numerator and denominator of PML condition in x direction defined in equation 16, other PML-related variables have similar meanings. Dxfm is the forward derivative operator of x (e.g., equation 9), Dybm and Dzbm are backward derivative operators of y and z (e.g., equation 10). C11, C12, and C13 are three of the five non-zero values of the components of the matrix of elastic moduli in the case of transverse isotropy.

2.3 Moment tensor source implementation

A point source is generally utilized for the simulation of small local or near-regional earthquakes, where the dominant wavelength is much larger than the source dimensions [45]. A point displacement discontinuity (e.g., dislocation) is assumed at the source, which can be mathematically represented with the body-force term in the equation of motion for the continuous medium [46]. A moment tensor is a mathematical representation of a point seismic source characterized by nine pairs of force couples that act at a point and expressed as a symmetric second-order tensor $\mathbf{M}$ [47]. The tensor component m_{ij} is a force couple of opposing forces applied along the i axis and situated along the j axis. Combined with the Green's function for seismic response of specific media, the moment tensor can be used to compute the corresponding displacement u due to an arbitrary source mechanism as follows

$$u_i = m_{jk} G_{ij,k} * s(t), \tag{11}$$

where $G_{ij,k}$ is the spatial derivative of the Green's function, $s(t)$ is the source-time function. The detailed equations of far-field displacement of P- and S-waves in a homogeneous isotropic elastic medium are [48]

$$u_i^P = \frac{1}{4\pi r \rho V_P^3} \gamma_i \gamma_j \gamma_k m_{jk} \dot{s}\left(t - \frac{r}{V_P}\right), \tag{12}$$

$$u_i^S = \frac{1}{4\pi r \rho V_S^3} \left(\delta_{ij} - \gamma_i \gamma_j\right) \gamma_k m_{jk} \dot{s}\left(t - \frac{r}{V_S}\right), \tag{13}$$

where u_i^P and u_i^S are the displacement at a distance r from the source, V_P and

V_S are P- and S-wave velocities, γ_i is the i th direction cosine of the ray path, and $\dot{s}$ is the time derivative of the source-time function.

The moment-tensor source can be implemented in two ways. One is loading the equivalent body-force term on momentum conservation equations, namely on particle velocity components [22, 49], and the other one is adding the body forces on stress components [23, 50]. The implementation of incremental stress is more straightforward between the two approaches and is adopted in this work. Shi et al. [39] provided a more reasonable formulation associated with four neighboring grid points of each shear stress component to obtain a symmetrical moment tensor solution (equation 15), while Li et al. [51] presented a simpler implementation setting all stress components at the single grid point (equation 14). Based on the configuration of nodes for different variables on the staggered-grid based FDM (Figure 1), we can obtain the moment tensor implementation with the stress components as following single point and multiple point schemes

$$\Delta \tau_{ij} = \frac{-m_{ij}\dot{s}(t)dt}{V},$$ (14)

$$\begin{cases} \Delta \tau_{ij} = \dfrac{-m_{ij}\dot{s}(t)dt}{V}, \ i = j \\ \Delta \tau_{ij} \big|_{(i\pm 1/2,\, j\pm 1/2)} = \dfrac{-m_{ij}\dot{s}(t)dt}{4V}, \ i \neq j \end{cases}$$ (15)

where $\Delta \tau$ is the incremental stress, $V = dx \cdot dy \cdot dz$ is the effective volume of the grid cell, dx, dy, dz are the spatial spacing and dt is the size of time steps. Both of the two schemes are included in our package, and the scheme with a single grid point is set as the default implementation.

2.4 Other implementation details

Boundary condition

To solve the problem of wave propagation through the subsurface, one must specify the appropriate initial and boundary conditions. The typical assumption is that of zero initial conditions, i.e., all wavefields used for modeling are all assumed to be at rest. The boundary condition deserves more attention and elaboration. In general, there are two types of boundary conditions, free surface boundary and absorbing boundary. The top surface can be treated as the free surface resembling the real scenario, namely air-solid interface for the land seismic and air-water interface in the case of the marine seismic. Our code package adopts the stress imaging technique [22, 42] to implement the free surface condition. The artificial absorbing boundary can be implemented either using the damping boundary condition or the perfectly matched layers (PML). The former is also called as the classical sponge method, in which the amplitudes are multiplied by a damping factor to eliminate spurious wave reflection at the boundaries [18]. The PML was initially proposed for electromagnetic wave propagation [19] and later utilized in elastic wave propagation by [20, 52, 53]. In this work, we use the classical (split) PML, in which all wavefields are first split into three orthogonal directions and then each is updated using the artificial damping provided by PML (equation 16).

Take the x component of particle velocity (v_x) as an example, formulation of discretized equations with PML as follows

$$v_x \mid^n = v_x \mid_x^n + v_x \mid_y^n + v_x \mid_z^n,$$

$$\begin{cases} v_x \mid_x^n = \dfrac{1}{1+\alpha_x dt/2}\left(\left(1-\alpha_x dt/2\right) v_x \mid_x^{n-1} + \dfrac{1}{\rho} D_x^+ \tau_{xx} \mid^{n-} \right), \\[2ex] v_x \mid_y^n = \dfrac{1}{1+\alpha_y dt/2}\left(\left(1-\alpha_y dt/2\right) v_x \mid_y^{n-1} + \dfrac{1}{\rho} D_y^- \tau_{xy} \mid^{n-} \right), \\[2ex] v_x \mid_z^n = \dfrac{1}{1+\alpha_z dt/2}\left(\left(1-\alpha_z dt/2\right) v_x \mid_z^{n-1} + \dfrac{1}{\rho} D_z^- \tau_{xz} \mid^{n-} \right), \end{cases} \qquad (16)$$

where $\alpha_x, \alpha_y, \alpha_z$ are the damping parameter along respective directions, the subscript and superscript of the variable denote the spatial direction and time step, respectively. For instance, $v_x \mid_x^n$ denotes the v_x component at x-direction and time step n. The remaining parameters have the same meanings as mentioned before. The damping parameter is calculated as $\alpha = \left(3V_p d^2 / 2W^3\right)\ln\left(R^{-1}\right)$, where d is the distance from the point to the inner boundary, W is the width of the boundary layer, and the theoretical reflection coefficient $R = 10^{-6}$ [20].

Numerical stability and grid dispersion

In FDM, the continuous derivatives are approximated by the numerical derivative operators and thus, numerical errors are inevitably introduced. These errors can introduce numerical dispersion and even cause instability in the numerical scheme of FDM. The relationship between the temporal and spatial grid spacing parameters (i.e., dt and dh) are coupled such that it affects the stability and the dispersion characteristics of the numerical scheme.

The numerical stability is achieved by constraining the timestep smaller than the time

taken by the wave travels between two adjacent grid points. For the 3D scenario, the timestep should fulfill the following Courant-Friedrichs-Lewy criterion [54]

$$dt \le \frac{dh}{V_{max}S\sqrt{3}}, \tag{17}$$

where V_{max} is the maximum velocity (among all directions) in the model, S is the summation over absolute values of Taylor coefficients. For fourth-order FD operator for the staggered grid scheme, $S = 27/24 + 1/24 = 7/6$.

The grid dispersion can be controlled by constraining the value of dx, and a general criterion can be obtained following the Nyquist-Shannon sampling theory [44]

$$dh \le \frac{\lambda_{min}}{w} = \frac{V_{min}}{wf_{max}}, \tag{18}$$

where λ_{min} denotes the minimum wavelength, w is the number of grid points per wavelength, V_{min} is the minimum velocity (among all directions) in the model and f_{max} is the maximum frequency of the source signal. A refinement of the spatial sampling of the model results in a more precise FD solution. The accuracy of the FD operator is determined by its length. For short FD operators, w should be chosen relatively large and thus require small spatial grid spacing, while grid spacing is allowed to be larger for high-order operators. A rule of thumb to minimize the grid dispersion is that the shortest wavelength should be sampled by at least five or six grid points to keep the numerical dispersion error below 5 % level [42, 55, 56]. Bohlen et al. [44] provided

more conservative conditions to avoid grid dispersion, e.g., $w=8$ and $w=5$ for a fourth- and tenth-order FD operator, respectively.

3 Architecture of the package

The basic architecture of the code package and an exemplary implementation are summarized in Figure 3, and Figure 4. For each specific case, the simulation can be separated into three parts as input calculation, and output. The basic steps to conduct seismic modeling are as follows:

● Initialize and setup the *FDwave3D* code.

● Define the model by assigning stiffness coefficients for the media.

● Define the source wavelet signature and the source mechanism.

● Select and setup the source and receiver geometry.

● Check the potential numerical stability and grid dispersion issues.

● Select the boundary condition.

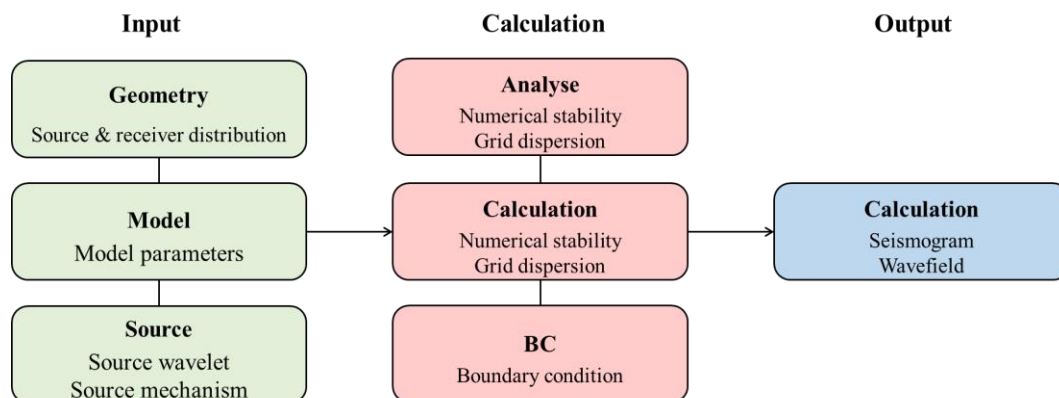● Carry out the simulation and show the results.

Figure 3. The basic architecture of *FDwave3D*: Light green, red, and blue boxes represent the folder names and functions of input, calculation, and output part of the simulation workflow.

```
%% Initialization
% Set path of FDwave3D package
% Add the code folder to the current command space
% Load model parameters P-wave velocity (vp), S-wave velocity (vs), density, etc.
% Other necessary parameters, e.g., the order of spatial derivative operators.
```

```
%% Input
% Calculate elastic parameters from Thomsen's parameters
thomsen_parameters=[vp(i),vs(i),eps(i),gamma(i),delta(i)];
cc=thomsen_to_c(thomsen_parameters);

% 3D anisotropic models with horizontal layers
FDwave_model_n_3Dlayers_FulAni(varargin);

% Source wavelet
FDwave_source_ricker(varargin);
% Source mechanism
MT0=sqrt(1/3)*[1 0 0;0 1 0;0 0 1]; %ISO

% Source and receiver geometry
FDwave_3Dgeometry_src_single(varargin); %Source
FDwave_3Dgeometry_rec_st_line_surf(varargin); %Receiver
```

```
%% Calculation and output
% Numerical stability and grid dispersion check
FDwave_analyse_3Delastic(varargin);
% Boundary conditions
FDwave_bc_3Dselect(varargin) ;
```

```
% Simulation and store the seismograms and wavefields
FDwave_calculation_3Delastic_2N_vFulAni(varargin);
```

Figure 4. Setup of an exemplary implementation for *FDwave3D*.

To facilitate the understanding of the examples in this work (see the following section), we briefly introduce the respective scripts and functions in Table 3. The code package (see Code availability) has been tested with MATLAB R2016b in both Windows and Linux operating systems.

Table 2

A brief introduction of the code package *FDwave3D* and the respective scripts and

functions mentioned in the manuscript.

Purpose	Script Name
Scripts for running simulations on different models	
Homogeneous model	Simulation3_homo_downhole.m
Horizontally layered model	Simulation3_layer3_TI.m
Over thrust model	Simulation3_overthrust_TI.m
Comparison of computational costs	compare_cost.m
Useful function provided within package	
Numerical stability and grid dispersion check	FDwave_analyse_3Delastic.m
Calculate moment tensor using fault plane solution	FPgenMT.m
Boundary condition (Damp/Sponge, PML)	bc_3Ddamp.m, bc_3Dpml.m
FD solver for the TI case	FDwave_calculation_3Delastic_2N_vTI.m
FD solver for the full anisotropic case	FDwave_calculation_3Delastic_2N_vFulAni.m

4 Application

Compared to active seismic modeling, the passive seismic sources generally lie in the subsurface with a higher dominant frequency content, and their source mechanisms are more complex than controlled sources, which are simple explosives or force sources. In this section, we demonstrated the reliability of the code with passive seismic or microseismic modeling over 3D homogeneous, layered, and overthrust models. The wavefield snapshots and records for different anisotropic media are analyzed and their computational costs (including processing time and memory cost) are compared.

First, we validate the accuracy of the method and code by comparing the synthetic

seismograms with analytical solutions for a homogeneous and isotropic model. Then, two anisotropic models (a horizontally layered model and the overthrust model) from [39] are utilized to test the accuracy of the proposed FD operator. The detailed parameters used for simulation are listed in Table 3. We set the FD operator with second-order in time and tenth-order in space (i.e., $O\left(\Delta t^2, \Delta x^{10}\right)$) as the default scheme, which is also consistent with [39].

Table 3

List of parameters used for FD seismic wave simulation.

Parameter	Symbol	3D Models		
		Homogenous	Horizontally layered	Overthrust
Grid spacing	dh	2.5 m	10 m	10 m
Time spacing	dt	0.0003 s	0.0005 s	0.0005 s
Total number of nodes	$nx \times ny \times nz$	$121 \times 121 \times 121$	$341 \times 341 \times 291$	$401 \times 401 \times 94$
Total time steps	nt	801	2401	2001
Receiver spacing	dr	Downhole line 10 m	Downhole line 10 m	Surface line 10 m
Source wavelet	$s(t)$	Ricker	Ricker	Ricker
Source central frequency	f_0	60 Hz	30 Hz	30 Hz
Source moment tensor	$\mathbf{M}$	$m_{xy} = m_{yx} = 1;$ $m_{yz} = m_{zy} = -1$	$m_{xy} = m_{yx} = 1$	$m_{xy} = m_{yx} = 1$
Number of PML layers	N_{PML}	20	20	20
Anisotropic parameters	ε γ δ	Isotropic	In the middle layer (0.334, 0.575, 0.73)	Around the source (0.334, 0.575, 0.73)

4.1 Homogenous and isotropic model

The homogeneous model size is 200 m × 200 m × 200 m, with the spatial and temporal spacing are $dx = 2.5\,m$ and $dt = 0.0003\,s$. The velocities of the model are $v_p = 3000\,m/s$, $v_p/v_s = 1.67$, and the density is $\rho = 2500\,kg/m^3$. The seismic source is located at (100 m, 100 m, 200 m). A downhole array with 15 receivers is deployed at the lateral position of $(x = 0, y = 0)$ to record the seismic data. Other parameters are listed in Table 3. In order to validate our code, we compare synthetic seismograms with corresponding analytical solutions (equations 12 and 13). The derivatives of the far-field displacement with respect to time in the x-direction are compared with the synthetic velocity components. The error between the compared traces is quantified using the root-mean-square (RMS) error ($\sqrt{\sum_{nt} \left(v_x^{FD} - v_x^{analytical} \right)^2 \big/ nt}$, where nt is the total number of time steps of each trace). As shown in Figure 5, the synthetic waveforms show good agreement with the analytical solution, and there is no obvious difference for the normalized amplitude and seismic phases between the two approaches.
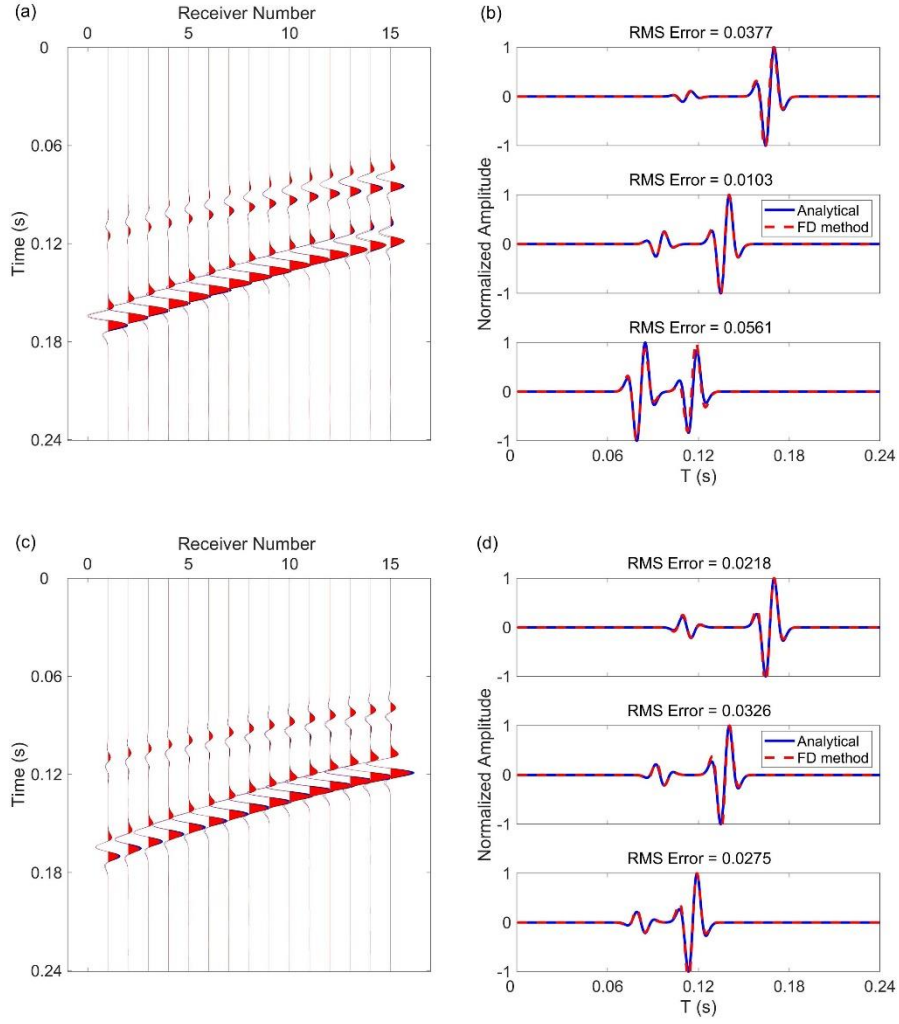
Figure 5. Comparison of synthetic seismograms with analytical solutions of two double-couple sources. (a) and (b) are results of a strike-slip source with moment tensor $\mathbf{M} = 1/\sqrt{2}\,(0\ 1\ 0; 1\ 0\ 0; 0\ 0\ 0)$, (c) and (d) are results of a dip-slip source with moment tensor $\mathbf{M} = 1/\sqrt{2}\,(0\ 0\ 0; 0\ 0\ \text{-}1; 0\ \text{-}1\ 0)$.

4.2 Horizontally layered model

A horizontally layered model with the size of 3000 m × 3000 m × 2500 m is tested in this section. The thickness of the three layers are 750 m, 1000 m, and 750 m, and

26

corresponding velocities and the density are $v_p = [3724, 4640, 5854]\, m/s$, $v_s = [1944, 2583, 3251]\, m/s$, $\rho = [2450, 2490, 2680]\, kg/m^3$, respectively. The seismic source with the vertical strike-slip mechanism is located in the middle of the model. A downhole array with 251 receivers is deployed at the lateral position of $(x = 1700\ m, y = 1700\ m)$.

The VTI and HTI models are commonly used to simulate horizontal stratification, e.g., shale formations, and the rock with vertical fractures, respectively. Besides the isotropic model, a VTI layer and a HTI layer are also used to show the effects of seismic anisotropy on the seismic wavefield. The HTI medium is constructed by rotating the VTI medium anticlockwise along the Y-axis by 90∘, in which the Thomsen parameters are $\varepsilon = 0.334, \gamma = 0.575, \delta = 0.73$, as measured anisotropy in the clay shale [41].

The vertical wavefield slices of the particle velocity in the y-direction for the three models are shown in Figures 6a-c. The existence of layer boundaries produces transmitted waves, reflected waves, and converted waves, making the wavefield complicated. For the VTI and HTI models, strong anisotropy can be observed in the shape of the wavefront and there are obvious quasi P- and S-waves (as shown in Figures 6b and 6c). The corresponding seismograms of the downhole array for the three models are shown in Figures 6d-f. Compared with the seismograms in the isotropic case, the seismograms for the TI models are much more complicated due to S-wave splitting, and more reflected and converted waves. The presence of seismic anisotropy results in difficulty for seismic processing, e.g., seismic event detection and phase picking.
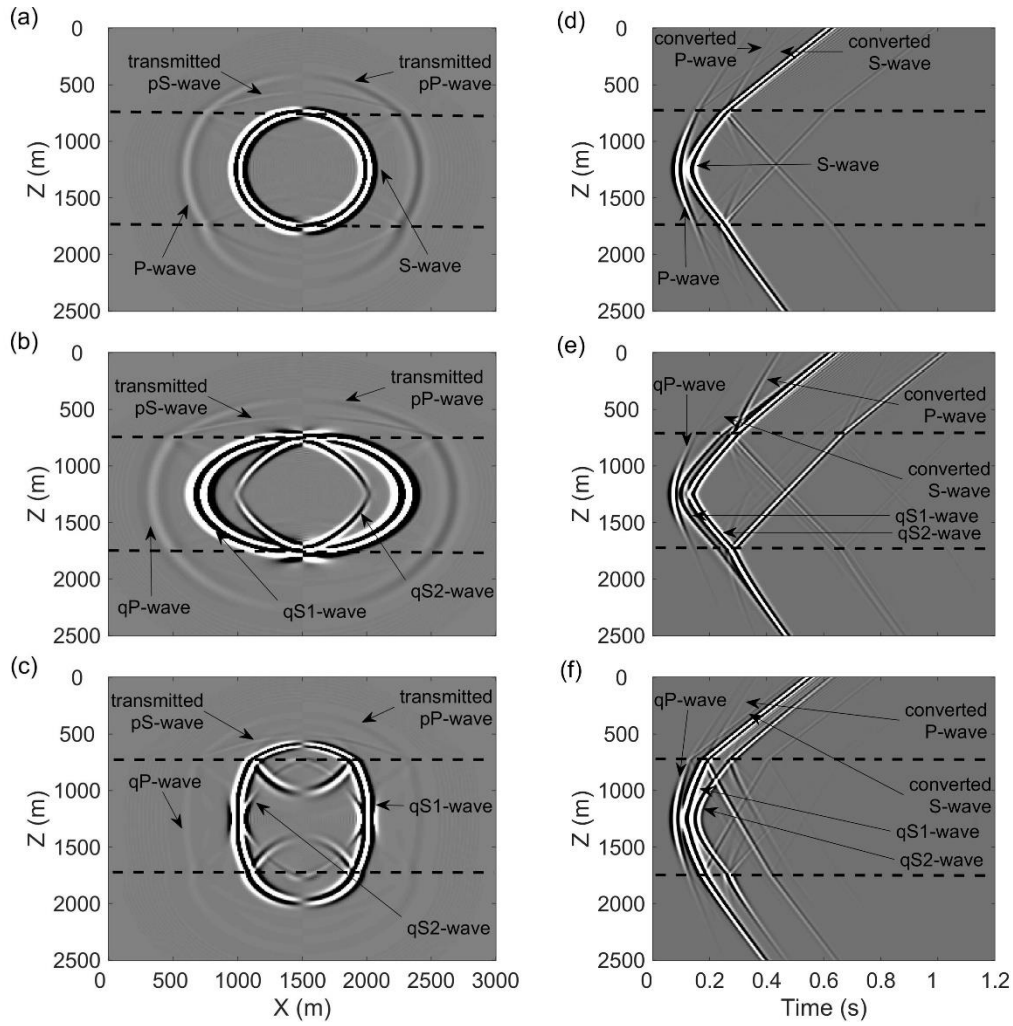
Figure 6. Wavefield snapshots of velocity component in the y-direction for isotropic (a), VTI (b), and HTI (c) models. The slices are taken at the simulation time of 0.23 s and lateral position of y=1500 m. The corresponding seismograms of the three different models are shown in (d), (e), and (f), respectively. Dashed lines show the boundaries of different layers. The figure is produced referring to Figures 7 and 8 in [39] for comparison, and the high degree of consistency between snapshots and seismograms provides cross-validation of the code.

4.3 Overthrust model

As the last example, we apply our code package to the benchmark SEG/EAGE

overthrust model [57], which is highly heterogeneous and widely used in exploration geophysics [58]. The P-wave velocity of the overthrust model is shown in Figure 7a. The overthrust model has a size of 401 × 401 × 94 nodes in the x-, y-, and z-directions with a grid spacing of 10 m. The same double-couple source with vertical strike-slip, as used in above horizontally layered model, is adopted and set in the middle of the model. We have considered three cases for this model as well, namely, isotropic, VTI, and HTI models. For TI models, the anisotropic region is set up around the source and the size is of 1000 m × 1000 m × 500 m (black lines in Figure 7). A surface array of 201 receivers is deployed at 2 km in the y-direction. The source-receiver geometry is shown in Figures 4b and 4c.
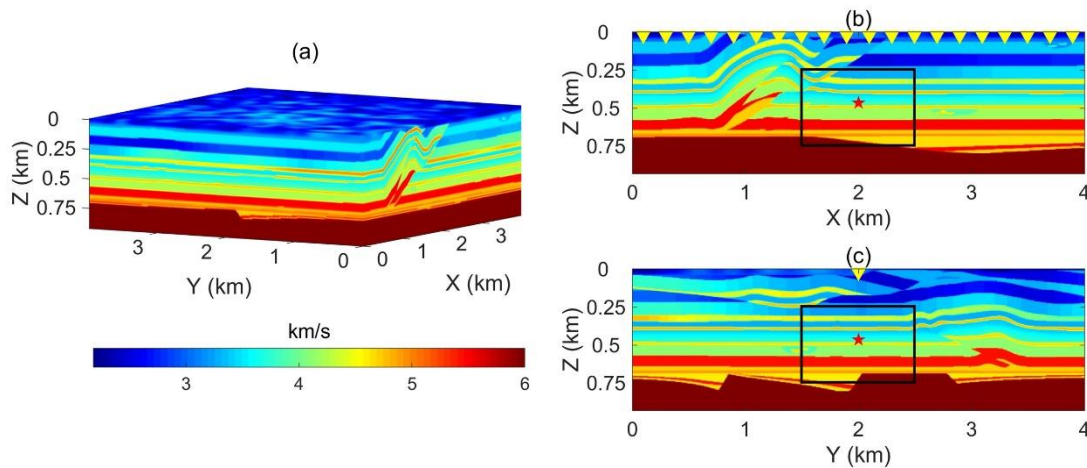

Figure 7. (a) P-wave velocity of the 3D overthrust model. (b) Velocity profile at 2 km in the y-direction. (c) Velocity profile at 2 km in the x-direction. The red star indicates the source position, the yellow reversed triangles indicate the surface array, and the black lines show the boundary of the anisotropic region in the model.

The vertical wavefield snapshots and the corresponding seismograms of the three models are shown in Figure 8. Due to seismic anisotropy, the wavefields of the

anisotropic models are much more complex than that of the isotropic model, especially in the anisotropic region (Figures 8a-c). This complexity arises from the S-wave splitting and velocity contrast between isotropic and anisotropic regions. A significant difference in the recorded seismograms can also be observed between the isotropic and TI models (Figures 8d-f).

5 Computational cost

The computation expense is quantified in terms of processing time and memory cost. The processing time is directly dependent on the size of the model, the number of time steps, the order of the derivative, and the type of boundary condition. A better measure is normalized processing time (total processing time/number of time steps), which is independent of the number of time steps. We want to investigate the effect of model size on computational efficiency, so we choose the same parameters for all simulations, including the same FD operator ($O\left(\Delta t^2, \Delta x^{10}\right)$) and the same PML boundary condition with a fixed thickness.
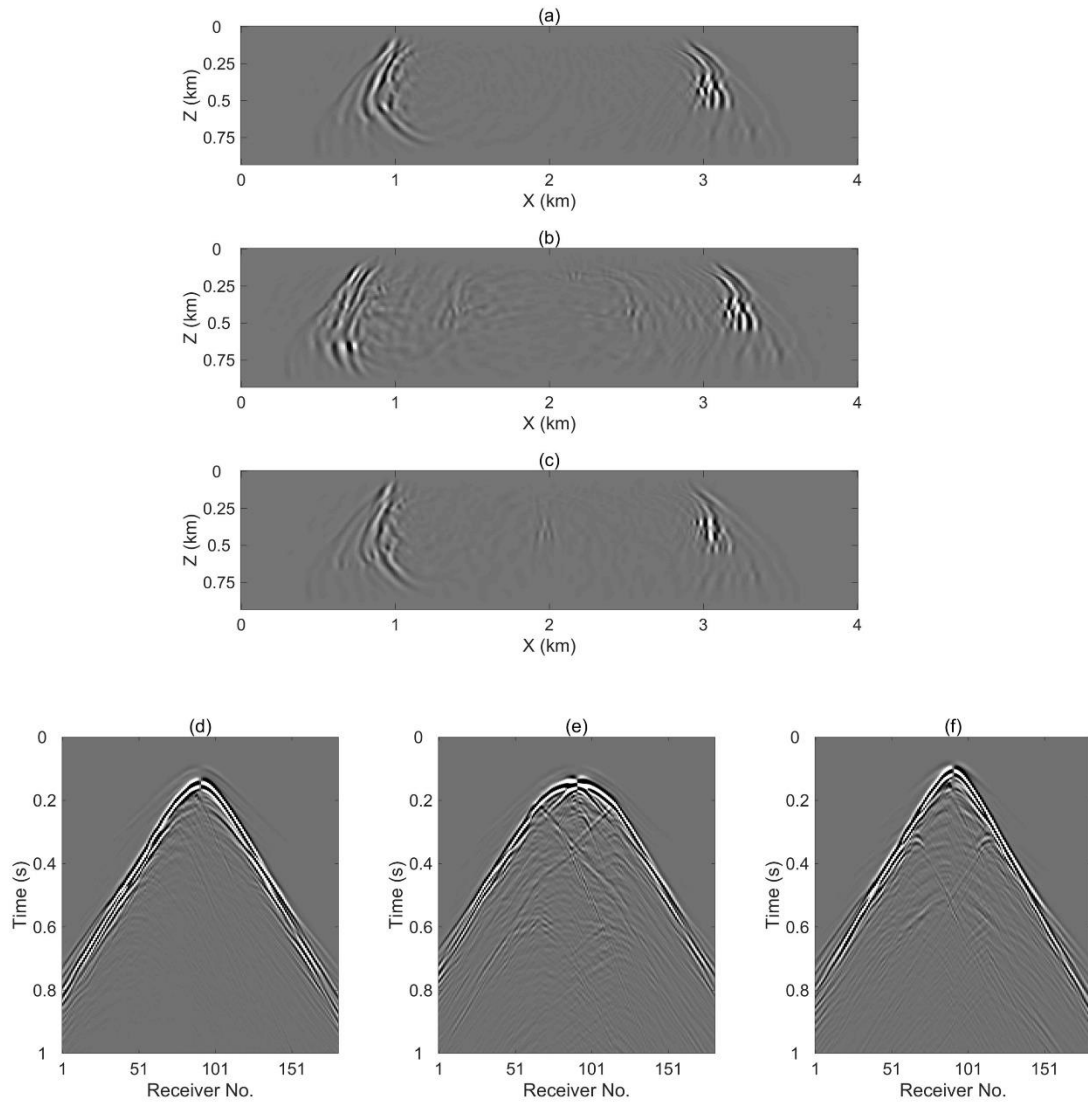
Figure 8. Wavefield snapshots of velocity component in the y-direction for isotropic (a), VTI (b), and HTI (c) models. The slices are taken at the simulation time of 0.5 s and lateral position of y=2 km. The corresponding seismograms of the surface arrays from the three different models are shown in (d), (e), and (f). The results are quite consistent with those in Figures 23 and 26 in [39].

31

The code package offers two solutions, pure-MATLAB codes and a C-MEX code. The former is convenient for users to manipulate and modify while the latter allows users to obtain synthetic results in a more efficient manner (in the context of MATLAB). The normalized processing time and memory cost for the aforementioned models are presented in Table 4. Two supplementary examples with the grid size of $171 \times 171 \times 171$ and $215 \times 215 \times 215$ are added to fill the size gap between the homogeneous and overthrust models. Theoretically, the normalized processing time increases linearly along with the total number of nodes in the double logarithmic coordinate, as shown in Figure 9. Please note that the related C++ code within the package is not fully optimized (e.g., vectorized or parallelized), which is beyond the scope of the current study. The tests are conducted on a standalone computer with 8 cores of Intel Xeon W-2123 CPU with the frequency of 3.60 GHz and 64 GB RAM in a Windows operating system.

Table 4

Normalized processing time (second) and memory cost (GB) for different codes and models.

Model parameter	Grid size	Code	Normalized processing time (second)	Memory cost (GB)
Homogeneous model	121×121×121	Pure-MATLAB	2.0	0.8
		C-MEX	0.7	0.8
	171×171×171	Pure-MATLAB	5.9	2.7
		C-MEX	2.4	2.8
	215×215×215	Pure-	12.3	5.0

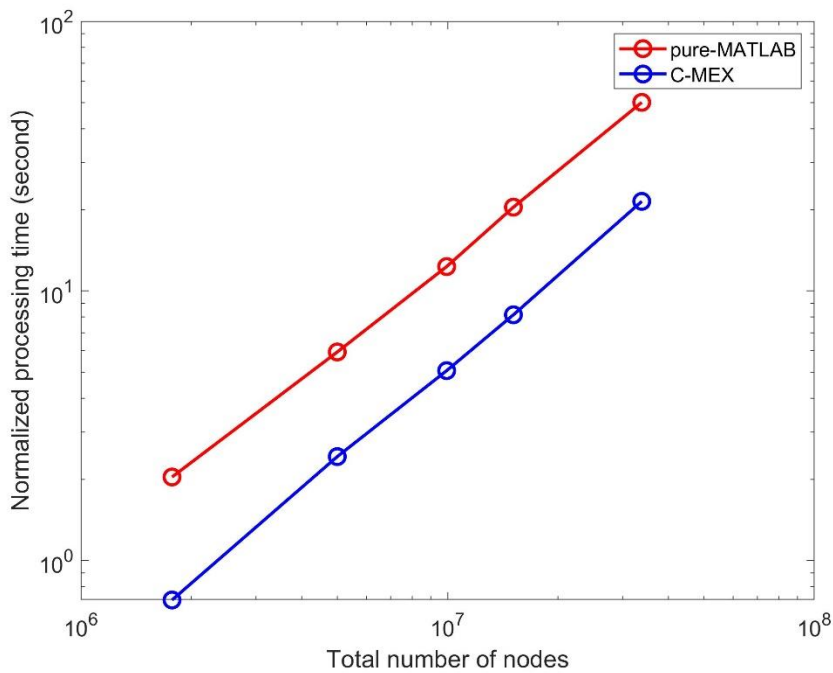|				
		MATLAB		
		C-MEX	4.9	5.3
Overthrust model	401×401×94	Pure-MATLAB	11.4	12.5
		C-MEX	4.6	13.5
Horizontally layered model	341×341×291	Pure-MATLAB	41.7	15.0
		C-MEX	18.0	18.5

Figure 9. Normalized processing time for different codes and models. The circles from the left to the right of each line correspond to the homogeneous model, two supplementary models, the overthrust model, and the horizontally layered model.

6 Conclusion

We developed an efficient MATLAB package for FD modeling of seismic waves in 3D anisotropic media. The code package provides various options for source implementations with arbitrary source mechanisms, boundary conditions, and variable accuracy (up to tenth-order) of the spatial derivative operators. In principle, the code can be applied to elastic wave propagation simulation in heterogeneous anisotropic media for both active and passive seismic surveys at all scales. Numerical examples have demonstrated the reliability of the method and the code package according to the test results on a standalone computer.

References

1. Sheriff, R.E., Geldart, L.P.: Exploration seismology. Cambridge University Press, Cambridge ; New York (1995)

2. Grechka, V., Yaskevich, S.: Azimuthal anisotropy in microseismic monitoring: A Bakken case study. GEOPHYSICS. 79, KS1–KS12 (2014). https://doi.org/10.1190/geo2013-0211.1

3. Stierle, E., Vavryčuk, V., Kwiatek, G., Charalampidou, E.-M., Bohnhoff, M.: Seismic moment tensors of acoustic emissions recorded during laboratory rock deformation experiments: sensitivity to attenuation and anisotropy. Geophys. J. Int. 205, 38–50 (2016). https://doi.org/10.1093/gji/ggw009

4. Foulger, G.R., Julian, B.R., Hill, D.P., Pitt, A.M., Malin, P.E., Shalev, E.: Non-double-couple microearthquakes at Long Valley caldera, California, provide evidence for hydraulic fracturing. Journal of Volcanology and Geothermal Research. 132, 45–71 (2004). https://doi.org/10.1016/S0377-0273(03)00420-7

5. Šílený, J., Hill, D.P., Eisner, L., Cornet, F.H.: Non–double-couple mechanisms of microearthquakes induced by hydraulic fracturing. Journal of Geophysical Research: Solid Earth. 114, B08307 (2009). https://doi.org/10.1029/2008JB005987

6. Meek, R., Hull, R.A., Von der Hoya, A., Eaton, D.: 3-D Finite Difference Modeling of Microseismic Source Mechanisms in the Wolfcamp Shale of the Permian Basin. Presented at the Unconventional Resources Technology Conference (URTeC) , San Antonio, Texas, USA (2015)

7. Hobro, J., William, M., Calvez, J.L.: The finite-difference method in microseismic modeling: Fundamentals, implementation, and applications. Leading Edge. 35, 362–366 (2016)

8. Rodríguez-Pradilla, G., Eaton, D.W.: Finite-difference modelling of microseismicity associated with a hydraulic-fracturing stimulation in a coalbed methane reservoir. First Break. 36, 41–48 (2018)

9. Carcione, J.M., Herman, G.C., ten Kroode, A.P.E.: Seismic modeling. GEOPHYSICS. 67, 1304–1325 (2002). https://doi.org/10.1190/1.1500393

10. Moczo, P., Kristek, J., Gális, M.: The finite-difference modelling of earthquake motions: waves and ruptures. Cambridge University Press, New York (2014)

11. Carcione, J.M.: Wave fields in real media: wave propagation in anisotropic, anelastic, porous and electromagnetic media. Elsevier, Amsterdam (2015)

12. Elsherbeni, A.Z., Demir, V.: The finite-difference time-domain: method for electromagnetics with MATLAB simulations. SciTech Publishing, an imprint of the IET, Edison, NJ (2016)

13. Cui, X., Lines, L., Krebes, E.S., Peng, S.: Seismic Forward Modeling of Fractures and Fractured Medium Inversion. Springer Singapore, Singapore (2018)

14. Bohlen, T.: Parallel 3-D viscoelastic finite difference seismic modelling. Computers & Geosciences. 28, 887–899 (2002). https://doi.org/10.1016/S0098-3004(02)00006-7

15. Torberntsson, K., Stiernström, V., Mattsson, K., Dunham, E.M.: A finite difference method

for earthquake sequences in poroelastic solids. Comput Geosci. 22, 1351–1370 (2018). https://doi.org/10.1007/s10596-018-9757-1

16. Vireux, J.: P-SV wave propagation in heterogeneous media: velocity stress finite-difference method. Geophysics. 51, 889–901 (1986)

17. Saenger, E.H., Gold, N., Shapiro, S.A.: Modeling the propagation of elastic waves using a modified finite-difference grid. Wave Motion. 31, 77–92 (2000). https://doi.org/10.1016/S0165-2125(99)00023-2

18. Cerjan, C., Kosloff, D., Kosloff, R., Reshef, M.: A nonreflecting boundary condition for discrete acoustic and elastic wave equations. GEOPHYSICS. 50, 705–708 (1985). https://doi.org/10.1190/1.1441945

19. Berenger, J.-P.: A perfectly matched layer for the absorption of electromagnetic waves. Journal of Computational Physics. 114, 185–200 (1994). https://doi.org/10.1006/jcph.1994.1159

20. Collino, F., Tsogka, C.: Application of the perfectly matched absorbing layer model to the linear elastodynamic problem in anisotropic heterogeneous media. Geophysics. 66, 294–307 (2001)

21. Saenger, E.H., Bohlen, T.: Finite-difference modeling of viscoelastic and anisotropic wave propagation using the rotated staggered grid. GEOPHYSICS. 69, 583–591 (2004). https://doi.org/10.1190/1.1707078

22. Graves, R.W.: Simulating seismic wave propagation in 3D elastic media using staggered-grid finite differences. Bulletin of the Seismological Society of America. 86, 1091–1106 (1996)

23. Pitarka, A.: 3D elastic finite-difference modeling of seismic motion using staggered grids with nonuniform spacing. Bulletin of the Seismological Society of America. 89, 54–68 (1999)

24. Sheen, D.-H., Tuncay, K., Baag, C.-E., Ortoleva, P.J.: Parallel implementation of a velocity-stress staggered-grid finite-difference method for 2-D poroelastic wave propagation. Computers & Geosciences. 32, 1182–1191 (2006). https://doi.org/10.1016/j.cageo.2005.11.001

25. Thorbecke, J.W., Draganov, D.: Finite-difference modeling experiments for seismic interferometry. GEOPHYSICS. 76, H1–H18 (2011). https://doi.org/10.1190/geo2010-0039.1

26. Malkoti, A., Vedanti, N., Tiwari, R.K.: An algorithm for fast elastic wave simulation using a vectorized finite difference operator. Computers & Geosciences. 116, 23–31 (2018). https://doi.org/10.1016/j.cageo.2018.04.002

27. Sharma, G., Martin, J.: MATLAB®: A Language for Parallel Computing. Int J Parallel Prog. 37, 3–36 (2009). https://doi.org/10.1007/s10766-008-0082-5

28. Wüstefeld, A., Bokelmann, G., Zaroli, C., Barruol, G.: SplitLab: A shear-wave splitting environment in Matlab. Computers & Geosciences. 34, 515–528 (2008). https://doi.org/10.1016/j.cageo.2007.08.002

29. Yu, C., Zheng, Y., Shang, X.: Crazyseismic: A MATLAB GUI-Based Software Package for Passive Seismic Data Preprocessing. Seismological Research Letters. 88, 410–415 (2017). https://doi.org/10.1785/0220160207

30. Boyd, O.S.: An efficient Matlab script to calculate heterogeneous anisotropically elastic

wave propagation in three dimensions. Computers & Geosciences. 32, 259–264 (2006). https://doi.org/10.1016/j.cageo.2005.06.019

31. Martin, R., Komatitsch, D.: An unsplit convolutional perfectly matched layer technique improved at grazing incidence for the viscoelastic wave equation. Geophysical Journal International. 179, 333–344 (2009). https://doi.org/10.1111/j.1365-246X.2009.04278.x

32. Michéa, D., Komatitsch, D.: Accelerating a three-dimensional finite-difference wave propagation code using GPU graphics cards: Accelerating a wave propagation code using GPUs. Geophysical Journal International. 182, 389–402 (2010). https://doi.org/10.1111/j.1365-246X.2010.04616.x

33. Weiss, R.M., Shragge, J.: Solving 3D anisotropic elastic wave equations on parallel GPU devices. GEOPHYSICS. 78, F7–F15 (2013). https://doi.org/10.1190/geo2012-0063.1

34. Köhn, D., De Nil, D., Kurzmann, A., Przebindowska, A., Bohlen, T.: On the influence of model parametrization in elastic full waveform tomography. Geophysical Journal International. 191, 325–345 (2012). https://doi.org/10.1111/j.1365-246X.2012.05633.x

35. Rubio, F., Hanzich, M., Farrés, A., de la Puente, J., María Cela, J.: Finite-difference staggered grids in GPUs for anisotropic elastic wave propagation simulation. Computers & Geosciences. 70, 181–189 (2014). https://doi.org/10.1016/j.cageo.2014.06.003

36. Maeda, T., Takemura, S., Furumura, T.: OpenSWPC: an open-source integrated parallel simulation code for modeling seismic wave propagation in 3D heterogeneous viscoelastic media. Earth, Planets and Space. 69, (2017). https://doi.org/10.1186/s40623-017-0687-2

37. Fabien-Ouellet, G., Gloaguen, E., Giroux, B.: Time-domain seismic modeling in viscoelastic media for full waveform inversion on heterogeneous computing platforms with OpenCL. Computers & Geosciences. 100, 142–155 (2017). https://doi.org/10.1016/j.cageo.2016.12.004

38. Zhu, T.: Numerical simulation of seismic wave propagation in viscoelastic-anisotropic media using frequency-independent Q wave equation. GEOPHYSICS. 82, WA1–WA10 (2017). https://doi.org/10.1190/geo2016-0635.1

39. Shi, P., Angus, D., Nowacki, A., Yuan, S., Wang, Y.: Microseismic Full Waveform Modeling in Anisotropic Media with Moment Tensor Implementation. Surv Geophys. 39, 567–611 (2018). https://doi.org/10.1007/s10712-018-9466-2

40. Chapman, C.H.: Fundamentals of seismic wave propagation. Cambridge University Press, New York (2004)

41. Thomsen, L.: Weak elastic anisotropy. GEOPHYSICS. 51, 1954–1966 (1986). https://doi.org/10.1190/1.1442051

42. Levander, A.R.: Fourth-order finite-difference P-SV seismograms. GEOPHYSICS. 53, 1425–1436 (1988). https://doi.org/10.1190/1.1442422

43. Igel, H., Mora, P., Riollet, B.: Anisotropic wave propagation through finite-difference grids. GEOPHYSICS. 60, 1203–1216 (1995). https://doi.org/10.1190/1.1443849

44. Bohlen, T., De Nil, D., Koehn, D., Jetschny, S.: SOFI3D - Seismic modeling with finite differences 3D - Acoustic and viscoelastic version. Karlsruhe Institute of Technology, Karlsruhe, Germany (2015)

45. Jost, M.L., Herrmann, R.B.: A student's guide to and review of moment tensors. Seismological Research Letters. 60, 37–57 (1989). https://doi.org/10.1785/gssrl.60.2.37

46. Burridge, R., Knopoff, L.: Body force equivalents for seismic dislocations. Bulletin of the Seismological Society of America. 54, 1875–1888 (1964)

47. Gilbert, F.: Excitation of the normal modes of the Earth by earthquake sources. Geophys J Int. 22, 223–226 (1971)

48. Aki, K., Richards, P.G.: Quantitative seismology. University Science Books, Sausalito (2002)

49. Li, H.J., Wang, R.Q., Cao, S.Y.: Microseismic forward modeling based on different focal mechanisms used by the seismic moment tensor and elastic wave equation. J Geophys Eng. 12, 155–166 (2015)

50. Li, D., Helmberger, D., Clayton, R.W., Sun, D.: Global synthetic seismograms using a 2-D finite-difference method. Geophysical Journal International. 197, 1166–1183 (2014). https://doi.org/10.1093/gji/ggu050

51. Li, L., Chen, H., Wang, X.M.: Numerical simulation of microseismic wavefields with moment-tensor sources. In: 2016 Symposium on Piezoelectricity, Acoustic waves, and Device Applications. pp. 339–343 (2016)

52. Chew, W.C., Liu, Q.H.: Perfectly matched layers for elastodynamics: a new absorbing boundary condition. J. Comp. Acous. 04, 341–359 (1996). https://doi.org/10.1142/S0218396X96000118

53. Komatitsch, D., Martin, R.: An unsplit convolutional perfectly matched layer improved at grazing incidence for the seismic wave equation. GEOPHYSICS. 72, SM155–SM167 (2007). https://doi.org/10.1190/1.2757586

54. Courant, R., Friedrichs, K., Lewy, H.: On the Partial Difference Equations of Mathematical Physics. IBM J. Res. & Dev. 11, 215–234 (1967). https://doi.org/10.1147/rd.112.0215

55. Robertsson, J.O.A., Blanch, J.O., Symes, W.W.: Viscoelastic finite-difference modeling. GEOPHYSICS. 59, 1444–1456 (1994). https://doi.org/10.1190/1.1443701

56. Moczo, P.: 3D Fourth-Order Staggered-Grid Finite-Difference Schemes: Stability and Grid Dispersion. Bulletin of the Seismological Society of America. 90, 587–603 (2000). https://doi.org/10.1785/0119990119

57. Aminzadeh, F., Jean, B., Kunz, T.: 3-D salt and overthrust models. Society of Exploration Geophysicists (1997)

58. Virieux, J., Operto, S.: An overview of full-waveform inversion in exploration geophysics. GEOPHYSICS. 74, WCC1–WCC26 (2009). https://doi.org/10.1190/1.3238367